Structural determination and kinetic analysis of the Transketolase from Vibrio vulnificus reveal unexpected cooperative behavior

Rainier-Numa Georges, Lionel Ballut, Guillaume Octobre, Arnaud Comte, Laurence Hecquet, Franck Charmantray, Bastien Doumèche

Doumeche Bastien (Orcid ID: 0000-0003-3458-1029)

RESEARCH ARTICLE

Protein Science
DOI10.1002/pro.4884

Structural determination and kinetic analysis of the Transketolase from *Vibrio vulnificus* reveal unexpected cooperative behavior

Rainier-Numa Georges, [1‡] *Lionel Ballut,* [2‡] *Guillaume Octobre,* [1] *Arnaud Comte,* [1] *Laurence Hecquet,*[3] *Franck Charmantray,* [3*] *Bastien Doumèche* [1*]

[1] Univ Lyon, Université Claude Bernard Lyon 1, CNRS, ICBMS UMR5246, 69622 Villeurbanne, France

[2] Molecular Microbiology and Structural Biochemistry, UMR 5086, CNRS-Université de Lyon, F-69367 Lyon, France

[3] Université Clermont Auvergne, CNRS, SIGMA Clermont, Institut de Chimie de Clermont-Ferrand (ICCF) F-63000 Clermont-Ferrand (France)

KEYWORDS: Transketolase, enzyme kinetic, cooperativity, structure, docking, inhibitor, two-substrate mechanism.

This article has been accepted for publication and undergone full peer review but has not been through the copyediting, typesetting, pagination and proofreading process which may lead to differences between this version and the Version of Record. Please cite this article as doi: 10.1002/pro.4884© 2023 The Protein Society
Received: Sep 21, 2023;Revised: Dec 07, 2023;Accepted: Dec 20, 2023

ABSTRACT

Vibrio vulnificus (*vv*) is a multidrug-resistant human bacterial pathogen whose prevalence is expected to increase over the years. Transketolases (TK), transferases catalyzing two reactions of the non-oxidative branch of the pentose-phosphate pathway and therefore linked to several crucial metabolic pathways, are potential targets for new drugs against this pathogen. Here, the *vv*TK is crystallized and its structure is solved at 2.1 Å. A crown of 6 histidyl residues is observed in the active site and expected to participate in the thiamine pyrophosphate (cofactor) activation. Docking of fructose-6-phosphate and ferricyanide used in the activity assay, suggests that both substrates can bind vvTK simultaneously. This is confirmed by steady-state kinetics showing a sequential mechanism, on the contrary to the natural transferase reaction which follows a substituted mechanism. Inhibition by the I38-49 inhibitor (2-(4-ethoxyphenyl)-1-(pyrimidin-2-yl)-1H-pyrrolo[2,3-b]pyridine) reveals for the first time a cooperative behavior of a TK and docking experiments suggest a previously undescribed binding site at the interface between the pyrophosphate and pyridinium domains.

ABBREVIATIONS

DHETPP, α,β-dihydroxyethylthiamin pyrophosphate; F6P, fructose-6-phosphate; PPP, pentose-phosphate pathway; TK, transketolase; TPP, thiamin pyrophosphate ; *vv*TK, transketolase from *Vibrio vulnificus*.

Introduction

Vibrio vulnificus is a halophilic gram-negative bacterium living in low salinity and warm water littorals (< 25% ppm NaCl and > 15 °C). [1, 2, 3] It is found in the south east of Asian and in the north of American littorals, together with others *Vibrio* species. At the horizon 2050, expansion of *Vibrio* species in these regions as well as in the north of Europe is expected due to the global warming. [2, 4, 5, 6]

Indeed, *V. vulnificus* is the deadliest *Vibrio* specie known nowadays regarding the number of deaths per infection while *V. cholerae* is the most prevalent specie. It infects seafood, especially shrimp and oysters in fish farms or in sea. [1, 2, 3] The first clinical case of *V. vulnificus* infection happened in the 70's. The prevalence of *V. vulnificus* infections still remains low; e.g. 1.237 per million worldwide but it has been increasing since the 70's. [1, 7] Infection by *V. vulnificus* is lethal in 51.6 % of the cases and is the most expensive digestive infection in the US. [3] Two modes of infections are possible: (i) a transdermal infection where the necrotic limb should be treated using antibiotics to prevent amputation and, (ii) a digestive infection that leads to septicemia with purpura and thoracic edema (without desquamations) happening in 24 h followed by fever, coma and possibly death in 72 h. [1] The origin of the multi-drug resistance of *V. vulnificus* is not well-known but it could result from antibiotic injection in waste water and further contamination of oceans and seas, combined with the capacity of this bacteria to transfer genes horizontally, in particular genes of antibiotic resistance, forming the *V. vulnificus* pangenome. [1, 3, 5] Therefore, new drugs directed against this bacterium should be searched. New antibiotics targets must be involved in several metabolic or cell signaling pathways, such as hub proteins, in order to inhibit important cell functions and cause pathogen death. Moreover, if the target is involved in a metabolic pathway rarely investigated (e.g. with few/no known drugs), it is likely that new molecular frameworks could be identified as lead compounds for new antibiotics. The pentose phosphate pathway (PPP) fulfills these conditions: (i) it is involved in NADPH, amino acids and nucleic acid precursors synthesis and (ii) few drugs target this pathway. The oxidative phase of PPP forms NADPH that limits the oxidative stress while the non-oxidative phase allows to regulate the biosynthesis of D-ribose-5-phosphate and D-sedoheptulose-7-phosphate, that are nucleic acid and amino acid precursors, respectively. [10, 11, 12, 13] The non-oxidative phase is totally reversible and is branched with glycolysis allowing a fine regulation of metabolites biosynthesis. [14] Only two enzymes are involved in this phase:

Transketolase (TK, E.C 2.2.1.1) and transaldolase (EC. 2.2.1.2). TK controls about 70 % of the PPP and catalyzes two of the three reactions of the non-oxidative part, while only 15 % of the PPP is controlled by D-glucose-6-phosphate dehydrogenase, making TK ideal for targeting the PPP. [15, 16] TK was proposed as a potential target in the search of new drug against the pathogen *Plasmodium falciparum*. [17, 18] In *Mycobacterium tuberculosis*, survival and pathogenicity is dependent of arabinogalactane, a heteropolysaccharide of the cell wall, derived from D-ribose-5-phosphate synthetized in the PPP. [19] Moreover, Human TK is able to discriminate TPP from 2'methyl-thiamnie pyrophosphate while *Escherichia coli* TK (*ec*TK) is not, evidencing the difference of selectivity between both enzymes. [20] These (still rare) examples from the literature strongly suggest that the PPP pathway is worth of investigation for discovery of new drugs against bacteria.

In the classical PPP, TK transfers two carbons units from a phosphorylated ketose donor (D-xylulose-5-phosphate) to a phosphorylated aldose acceptor (D-ribose-5-phosphate or D-eythrose-4-phosphate), leading to a phosphorylated aldose (D-glyceraldehyde-3-phosphate) and to a phosphorylated ketose (D-sedoheptulose-7-phosphate or D-fructose-6-phosphate (F6P)), according to a reversible substituted (ping-pong) mechanism with thiamin pyrophosphate (TPP) as cofactor. [13] During the reaction, the two carbons unit from the ketose donor is transiently grafted on the C2-carbanion of the thiazolium ring of TPP, forming α,β-dihydroxyethylthiamin pyrophosphate (DHETPP) while the aldose product is released. [21] The two carbons units are further transferred to the aldose acceptor from DHETPP to give the ketose product. This reaction is herein referred as the transferase reaction.

The TK of *V. vulnificus* (*vv*TK) has not been characterized up-to-date, with the exception of its uniport entry (Q7MDD4), but yet described TK share common structural features. They are homodimers with two active sites located in cavities formed between each monomer, [22] the latter being associated with each other in an "interlocking V-shaped" structure. [23] The two active sites bind a divalent cation (Ca^{2+}, Mn^{2+}, Mg^{2+}…) linked to the pyrophosphate group of TPP. [13, 24, 25] TK monomers have three domains consisting of 5-to-6 β-strands forming a β-sheet surrounded by α-helices (Rossmann fold). The first domain binds the pyrophosphate moiety of TPP and is therefore called pyrophosphate domain (PP domain). The second domain is the pyrimidine domain (Pyr domain) and is very closed to the PP domain because it interacts with the pyrimidine ring of the TPP. PP and Pyr

domains contribute together to the arrangement of the active site when TK chains interact together to form the homodimer. The last domain is the C-terminal domain. Regarding this structure, TPP is not only a cofactor but also a structural partner as it promotes homodimer association by taking place in a hydrophobic pocket formed by both chains. [26] It adopts a V-shape geometry characteristic for all TPP-dependent enzymes. [21]

Several TK inhibitors have been reported in the literature and are competitive for TPP binding (oxythiamine K_i = 1.4 mM, [27] thiamine K_i = 34 mM, [28] pyrophosphate K_i = 0.28 mM [28]), or competitive for the donor substrate binding (hydroxyphenylpyruvate (K_i = 3 mM)) for the TK from *Saccharomyces cerevisiae* (*sc*TK).[29] D-arabinose-5-phosphate inhibits *ec*TK with a K_i of 6 mM.[30] *In silico* screening have allowed to identify inhibitors of the Human TK, all based on diphenyl urea derivatives (IC_{50} comprised between 0.1 and 0.2 mM)[31] and a docking study on the TK from *Plasmodium falciparum* has led to a family of 4-anilinoquinoline triazine derivatives with IC_{50} comprised between 0.072 and 0.085 mM [24] with still unknown inhibition mechanism. This highlights the fact that TK are still understudied targets in the fight against pathogens regarding the low number of available synthetic inhibitors. Obviously, this requires characterization of TK structures, kinetic mechanisms and inhibitor mode of action, including *vv*TK.

Several assays have been developed to determine TK kinetic constants using a ketose/aldose substrate couple such as D-xylulose-5-phosphate/ribose-5-phosphate or L-erythrulose/D-ribose-5-phopshate. The D-glyceraldehyde-3-phosphate (G3P) product is then reduced by a G3P dehydrogenase [32] or an alcohol dehydrogenase using NADH as co-substrate. [33, 34]

Alternatively, an assay based on the oxidation of the DHETPP intermediate by ferricyanide ($Fe(CN)_6^{3-}$) is also described, although less used. [35] After reaction with the ketose donor and the aldose release, two molecules of $Fe(CN)_6^{3-}$ oxidize DHETPP in the presence of a water molecule leading to two $Fe(CN)_6^{4-}$ and glyoxylate (**equation 1**). Enzymatic activity could be measured by monitoring the decrease of the $Fe(CN)_6^{3-}$ absorbance at 420 nm (ε_M^{420nm} ~1000 $M^{-1}.cm^{-1}$) or by oxidizing $Fe(CN)_6^{4-}$ with a carbon electrode. [36] Nevertheless, the kinetic mechanism of this reaction is poorly understood.

Equation 1:

$$\text{Ketose } (C_n) + 2\ Fe(CN)_6^{3-} + H_2O \rightarrow \text{aldose } (C_{n-2}) + \text{glyoxylate } (C_2) + 2\ Fe(CN)_6^{4-} + 3\ H^+$$

An electrochemical assay based on this reaction was used to screen a chemical library allowing the identification of a new inhibitor of the *ec*TK (I38-49, **Supporting information**). [37, 38] Nevertheless, the proposed inhibition mechanism (partial mixed inhibition) was not totally satisfactory because the reaction steps involving ferricyanide are not fully understood.

In the present work, we obtain for the first time the structure of *vv*TK solved by X-ray crystallography. Its mechanism is further studied by steady-state kinetics using F6P and $Fe(CN)_6^{3-}$ as substrates. This study is complemented by inhibition studies using I38-49 and docking experiments. All these data are important for anticipating infection by a human pathogen which will be closely monitored in the near future.

Material and Methods

Reagents. Agar, bovine serum albumin, glycerol (≥ 99%), Hepes, imidazole, isopropyl β-D-1-thiogalactopyranoside (IPTG), Luria broth (LB) medium, sodium phosphate monobasic monohydrate, thiamine hydrochloride (≥ 99%), thiamine pyrophosphate (TPP, ≥ 95%) were purchased from Sigma. Ammonium sulfate was purchased from Merck. Bradford protein assay reagent was from Bio-Rad. Potassium chloride was from BDH. D-fructose-6-phosphate disodium salt (≥ 98%) was purchased at ABCR. Di-sodium hydrogenophosphate, potassium hexacyanoferrate (III) ($K_3Fe(CN)_6$) and sodium chloride were purchased from Prolabo. Ampicillin was from Roth.

Plasmid and strains. pET21b(+)-*vv*TK recombinant vector was synthetized by GeneScript® as follow: TK gene sequence from *V. vulnificus* was obtained from the protein sequence (UniProt: Q7MDD4) to which a TEV protease recognition sequence (ENLYFQ) [39] was added at the C-ter extremity. The resulting sequence was inserted into pET21b(+) vector between NdeI and XhoI restriction sites at 5' and 3' extremities, respectively. A vector-encoded 6×His-tag peptide sequence was present downstream of the XhoI restriction site. Codons optimization for *E. coli* was done by the algorithm of GenScript® and the recombinant vector was synthetized by the same company (pET21b(+)-*vv*TK).

E. coli BL21(DE3) were prepared in our lab. After 10 min on ice, they were transformed by a 45 sec heat shock at 42°C using 200 ng of recombinant vector (pET21b(+)-*vv*TK). After one hour of recovery in LB medium at 37 °C, bacteria were centrifuged at 10000 × g during 1 min and resuspended in 200 µL of fresh LB medium. Bacteria were then spread on LB-agar supplemented with 100 $\mu g.mL^{-1}$ ampicillin. Clones were grown at 37 °C overnight.

***vv*TK expression and purification.** A transformed clone was used for a pre-culture in LB medium (37°C, overnight) in the presence of 100 $\mu g.mL^{-1}$ ampicillin. Two-liter cultures were grown from a 1/100 dilution of the pre-culture in LB medium supplemented by 100 $\mu g.mL^{-1}$ ampicillin at 30 °C under agitation. Induction of the *vv*TK expression was done by adding IPTG (0.5 mM) and thiamine (10 µM) when the optical density at 600 nm reached a value of 0.6-0.8. [19] Cultures were maintained at 20°C for 20 h before bacteria were harvested by centrifugation (3000 × g) at 4°C, washed with deionized water and frozen at -80°C. Bacteria pellets were suspended in 50 mM pH 8.0 sodium phosphate supplemented by 300 mM NaCl and cells were disrupted by

sonication. Cell debris were eliminated by centrifugation at 6000 × g. Supernatant was clarified on Whatman #1 paper and *vv*TK was purified by affinity chromatography using a nickel His-trap FF prepacked column (5mL, GE Healthcare) mounted on an AKTA Start® chromatographic system. Elution was performed with an imidazole gradient (from 0 to 200 mM in 50 mM sodium phosphate pH 8.0 containing 300 mM NaCl). Fraction containing *vv*TK were collected and dialyzed overnight at 8°C against 4 L of 5 mM sodium phosphate buffer pH 8.0 containing 30 mM NaCl (8 kDa cut-off membrane, Spectra/Por 6 dialysis Membrane from Spectrum Lab). Finally, *vv*TK was precipitated by dialysis at 8°C against 1 L of 3 M ammonium sulfate for 5 h before storage at 4 °C. [40, 41]

Protein quantity was determined by Bradford assay and quality of the purification was controlled by SDS-PAGE analysis using 12% (w/v) polyacrylamide separation gel and 8% (w/v) polyacrylamide stacking gel.

Enzyme kinetics.

*vv*TK activity was measured using the assay described by Kochetov *et al.* [35] (equation 1) and D-fructose-6-phosphate (F6P) as ketose donor: *vv*TK stored in 3M ammonium sulfate was centrifuged during 2 min and, after discarding the supernatant, resuspended in 50 mM Hepes buffer pH 7.0, KCl 100 mM. Concentration was controlled by Bradford assay. Reactions were performed in 200 µL using 0-2 mM $Fe(CN)_6^{3-}$, 0-0.5 mM F6P, 2 mM $MgCl_2$, 0-0.2 mM TPP and 0.9 µM *vv*TK in a 96-well plate (Greiner Bio-one) at 37°C. Absorbance was recorded at 420 nm during 1 h at 37 °C using a Berthold Tristar 5 microtiter plate reader. Reactions were triggered by $Fe(CN)_6^{3-}$ addition and control reactions were obtained in the absence of F6P. Initial rate were corrected using control reaction (< 1.0 µM.min^{-1}). Reaction rates are expressed in µM.min^{-1} using response coefficient ($\varepsilon_M^{420nm} \times l$) of $Fe(CN)_6^{3-}$ (0.4725 mM^{-1} in these conditions). Specific activity was expressed as µmol of F6P converted to D-erythrose-4-phosphate (E4P) per minute and per milligram of *vv*TK.

Inhibition studies of *vv*TK by I38-49 (2-(4-ethoxyphenyl)-1-(pyrimidin-2-yl)-1H-pyrrolo[2,3-b]pyridine) [42] were performed using inhibitor concentrations of 0-400 µM. I38-49 was not found to react with $Fe(CN)_6^{3-}$ or $Fe(CN)_6^{4-}$. In all experiments, the conversion was verified to be below 10% to avoid underestimation of the reaction rate. Data plotting and kinetic analysis (linear and non-linear fitting) were done using Magicplot software (v3.0.1, www.magicplot.com).

Molecular modelling of *vv*TK including TEV cleavage site and 6×His-tag.

The introduced TEV sequence should form an alpha helix at the C-terminus of the recombinant *vv*TK. To verify that the TEV cleavage site and the 6×His tag did not impact the secondary structure, the latter was predicted using SOPMA (https://npsa.lyon.inserm.fr/cgi-bin/npsa_automat.pl?page=/NPSA/npsa_sopma.html).

*vv*TK-TEV-Histag structure was first modelized using Swiss-Model (02.01.2022 version, https://swissmodel.expasy.org/) [43, 44] using the *ec*TK structure as template (PDBid 2R8P) including the TEV cleavage site and the 6×His-tag. Model selection was done maximizing GMQE, QSQE metrics and sequence coverage. Hydrogen atoms position were predicted using MolProbity (v4.5.1, http://molprobity.biochem.duke.edu/). [45, 46] Asn, Gln and His flips were allowed and heteroatom-H bond-length were calculated on their electron-cloud. Each His residue tautomer and Asn and Gln residues rotamers were verified using PyMol (v2.5.2, https://pymol.org) to avoid steric clashes. [46] Energy minimization was performed with SPDB viewer v4.10 using GROMOS96 force field in order to enhance the model quality: a first steepest descent (200 steps), followed by a conjugate gradient (200 steps) and a second steepest descent (200 steps) were performed on the *vv*TK model. All software options were selected for minimization (bonds, angles, non-bounded, electrostatic, torsions, improper). [47] Model evaluation was performed using PROCHECK, [48] Verify 3D [49] and ERRAT [50] (02.07.2022 versions, https://saves.mbi.ucla.edu/). RMSD were obtained using PyMol (Schrödinger, [illegible]).

Crystallization of *vv*TK structure. The *vv*TK stored at 4 °C in 3 M ammonium sulfate was centrifugated during 2 min with a benchtop centrifuge. Supernatant was discarded and the enzyme was resuspended in 50 mM Hepes buffer pH 7.0, 100 mM KCl before desalting by gel-filtration chromatography (Hi-Prep 26/10 desalting prepacked column from GE Healthcare mounted on an AKTA Start® system) using the same buffer to remove ammonium sulfate traces. *vv*TK was concentrated using Microsep Advance centrifugal device (30 kDa cutoff, Pall) at 3220 × g at 4 °C during 45 min and TPP and $MgCl_2$ prepared in the same buffer were added to *vv*TK at final concentrations of 0.9 mM and 1.8 mM, respectively. Protein concentration was determined at 280 nm with a NanoDrop® system using the molar extinction coefficient of *vv*TK predicted by ProtParam ($\varepsilon_M^{280\ nm}$ = 100060 $M^{-1}.cm^{-1}$, 1.351 for 1 $g.L^{-1}$, 02.01.2022 version, https://web.expasy.org/protparam/). [51]

Crystallization screening conditions were carried out using the sitting-drop vapor-diffusion method using commercial crystallization kits. For screening, a Mosquito® crystallization robot (SPT Labtech) was employed using one protein/crystallization agent ratio (100 + 100 nL drops equilibrated against 70 µL in MRC Crystallization Plates (Molecular Dimensions)). *vv*TK (31 $mg.mL^{-1}$) led to crystal growth in 0.16 M calcium acetate, 0.08 M sodium cacodylate pH 6.5, 14.4% PEG 8000, 20% glycerol. Crystals were further cryo-protected in the same solution to which 15% ethylene glycol was added, and then harvested. X-ray diffraction data were collected at the ID23_1 beamline (ESRF, Grenoble) at a wavelength of 0.885600 Å. Data were indexed, integrated and scaled using XDS. [52] The phase problem was solved by molecular replacement using phenix.phaser [53] with herein constructed model. The experimental model was then built using Coot [54] and refinement was carried out using PHENIX. [53, 55, 56] Data collection and refinement statistics are shown in **Table 2**. PyMol (Schrödinger, LLC) was used to render the molecular structures.

Molecular docking of substrates and inhibitor on *vv*TK structure. Water molecules and nickel ion were discarded from the *vv*TK structure using PyMol to obtain a structure containing TPP and Mg^{2+}. For docking experiments with DHETPP, the structure of DHETPP was obtained from the structure of *S. cerevisae* TK (PDBid 1CPU) and aligned with the TPP in the *vv*TK structure. The TPP was discarded and the resulting PDB file was saved successively in PQR and then in PDBQT format files with Open Babel (v3.1.1, https://github.com/openbabel/openbabel/releases/tag/openbabel-3-1-1). [57] MMFF94 force field was used to calculate partial charges at pH 7.0. Ferricyanide SMILES code was obtained from PubChem (CID: 439210, https://pubchem.ncbi.nlm.nih.gov/) and formatted in PDB format with OpenBabel online with 3D coordinates generated at pH 7.0 (v2.3.2, http://www.cheminfo.org/Chemistry/Cheminformatics/FormatConverter/index.html). Structure of the cyclic and linear F6P were also obtained from PubChem (CID: 440641 and CID: 69507, respectively). AMDock (v1.5.2, https://github.com/Valdes-Tresanco-MS/AMDock-win) [58] was used with AMBER forcefield in AutoDock 4 using following parameters: exhaustiveness = 8, number of poses = 10, energy evaluation= 2500000, 10 runs, cluster tolerance = 2.0 and no ligand protonation. Mg^{2+} cation was maintained in the active site and pH was fixed at 7.0. For F6P docking experiment, the cube size was 42.0 Å and centered at the position x=-39.9 Å, y= 24.0 Å,

z=-19.5 Å. The box used for docking $Fe(CN)_6^{3-/4-}$ on *vv*TK containing TPP was 32.0 Å wide and was centered on coordinates x=-38.8 Å, y= 36.3 Å, z=-22.4 Å. In the case of *vv*TK containing DHETPP, the box was centered at the position x=-14.60 Å, y= 59.10 Å, z=11.10 Å (same size). The box used for the docking of I38-49 was 99 × 99 × 99 Å (maximum sized allowed by AMDock) to encompass the whole *vv*TK structure and to allow the binding of I38-49 at any position of the protein. In this case, the box was centered on coordinates x= 17 Å, y= 28 Å, z=-36 Å (**Supporting information**).

Results

***vv*TK expression and purification.** After cloning, expression in *E. coli* BL21(DE3) and lysis, *vv*TK is purified by affinity and eluted using 80 mM imidazole. The purification yield is 26 % and a main band at 70 kDa (expected molecular weight is 73891 kDa) is observed on the SDS-PAGE (**Supporting Information**). Around 94.0 mg of *vv*TK are purified from a 2 L culture with a specific activity of 0.102 $\mu mol.min^{-1}.mg^{-1}$ using F6P and $Fe(CN)_6^{3-}$ as substrates. When no TPP is added to the reaction media, no activity is measured meaning that *vv*TK is purified as an apoenzyme (e.g. without its cofactor).

Molecular modeling. vvTK was modeled by molecular threading, utilizing the structure of E. coli TK (PDBid 2R8P) by incorporating its own sequence into this structure. These two proteins share more than 30% of sequence identity ensuring a good quality of the *vv*TK model. Swiss-Model was the preferred tool for obtaining the vvTK dimer directly from the primary sequence. Detailed description of the modeling and metrics are provided in the **Supporting information**. As expected, the global fold of the model superimposed with the *E. coli* template.

Crystallisation.

Table 1: Data collection and refinement statistics.

Structure-ID	***vvTK***
Data collection	
Beamline	ID23-1
Wavelength (Å)	0.8856
Space group	P 1 2_1 1
Cell dimensions	
a, b, c (Å)	69.23 75.48 130.39
α, β, γ (°)	90.0 99.87 90.0
Resolution range (Å)	34.95 - 2.10
Highest resolution shell (Å)	2.1-2.2
Total reflections	245442

Unique reflections	76983
R_{meas} (%)	8.7 (89.6)
$CC_{1/2}$ (%)	99.7 (67.5)
I/σ(I)	11.66 (1.95)
Multiplicity	3.19 (3.19)
Completeness (%)	99.4 (99.6)
No. mol. /asymm. unit	2
Refinement	
R_{work}/R_{free} (%)	16.25 / 20.70
No. atoms	
Protein	10356
Ligand/ion	103
Water	715
Wilson B-factor (Å²)	35.07
Average B-factor (Å^2)	
Protein	37.30
Ligand/ion	40.85
Water	41.95
r.m.s.d.	
Bond lengths (Å)	0.007
Angles (°)	0.823
Ramachandran	
Favored (%)	97.26
Allowed (%)	2.74
Outliers (%)	0.0

Initial crystallization attempts were conducted in the presence of the tag. The TEV cleavage site was included with the intention of obtaining a native protein in case the tag interfered with crystallization. However, since the uncleaved protein allowed for the acquisition of a structure at a satisfactory resolution, and considering that the

presence of the tag seemed to stabilize the C-terminus through its interaction with a Nickel ion, the decision was made to retain the 6×His tag. Following the acquisition, integration, and reduction of the data, a resolution of 2.1 is maintained. The 3D model constructed earlier prove effective as a search model in the molecular replacement process. Following subsequent refinement steps, a final crystal structure is achieved at a resolution of 2.1 Å with R factors of 16.25% (R_{work}) and 20.7% (R_{free}) (**Figure 1**, **Table 2**).

The *vv*TK crystal and model exhibit a closed folding with an RMSD of 0.394 Å and form the classical Canadian ten , as described for other TK with a similar fold. This structural arrangement is in close proximity to other microbial TK that have been previously crystalized (RMSD < 1.0 Å), including *ec*TK, which was used as the template for modeling (**Supporting Information**). Interestingly, all residues from Met1 to His 678 are solved in the X-ray structure of chain A, including the 6×His-tag together with a nickel ion (*vide infra*). The chain B covers the residues Met 1 to His 674. The crystal includes the *vv*TK cofactors (two magnesium ions and two TPP molecules) added to the protein solution before crystallization (**Material and methods**). Additionally, ten ethylene glycol molecules from the crystallization solution are found in the crystal.

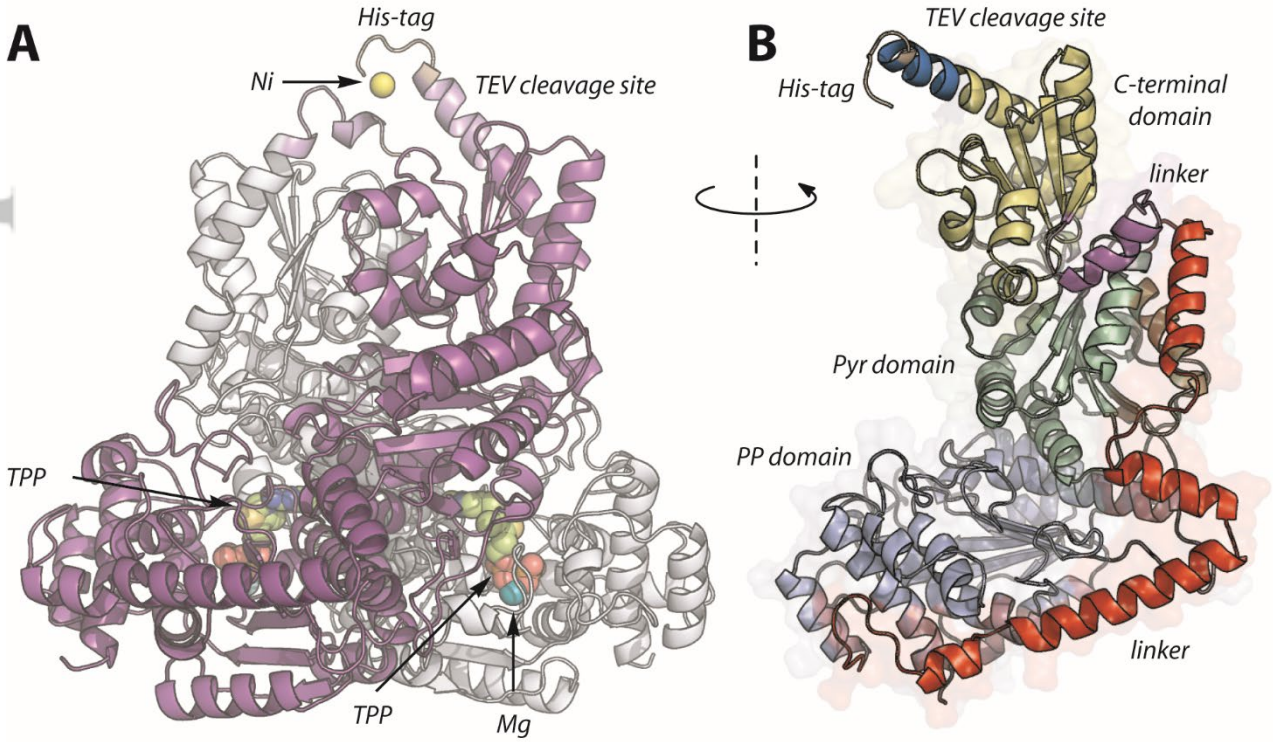

Figure 1: Structure of the *vv*TK obtained by X-Ray crystallography (A). Chain A is colored in white and chain B in purple. Both are shown as ribbon, TPP molecule is depicted as colored spheres, magnesium ions (Mg) are in light blue and nickel ion (Ni) is in yellow. His-tag and TEV protease recognition sites are in light pink. Heteroatoms in TPP are colored as follow: carbon in green, nitrogen in blue, oxygen in red, sulfur in yellow and phosphorous in orange. Figure is constructed using PyMol software. Single monomer of *vv*TK showing domains (B): from N-terminal to C-terminal extremities, one *vv*TK monomer is composed of PP domain (light blue), Pyr domain (light green) and C-terminal domain (light yellow). The linkers are shown in red between Pyr and PP domains and in purple between Pyr and C-terminal domains. TEV protease recognition site is colored in marine blue and His-tag in light brown. Structure is shown as ribbons together with a transparent surface and is rotated along the vertical axis compared to the dimer structure shown in A.

As predicted by the model, the *vv*TK shares common features with described bacterial TK from *E. coli* and *M. tuberculosis*. It forms a homodimer in an embedded V with C-terminal extremities oriented in the same direction (**Figure 1**A). The two subunits have an RMSD of 1.135 Å evidencing a perfect symmetry of the protein crystal. A single *vv*TK chain is formed by three domains separated by two linkers (**Figure 1**B).[19, 23] The PP domain (Met 1-Leu 275) contains the interaction site with the pyrophosphate (PP) moiety of TPP. The linker region (Gly 276-Ala 354) between PP and Pyr domains is formed by three helices in *vv*TK vs two in *M. tuberculosis* TK, the first helix being split in two in *vv*TK.[19] The second helix (Ser 294-Tyr 315) in *vv*TK is lacking in *H. sapiens* TK. This main difference between bacterial and human TK would affect the flexibility between PP and Pyr domains. The Pyr domain (Ser 355-Phe 517) contains the interaction sites with the pyridinium and thiazolium rings of TPP and a hydrophobic pocket around both TPP rings. This pocket is also formed by the PP domain of the other monomer (*vide supra*, **Supporting information**). The C-terminus domain (Tyr 540-Ala 663) allows the interaction between the two chains of the homodimer. All the domains have a Rossman fold as described for all other known TK.[22] Two TPP molecules are resolved in the X-ray structure evidencing the localization of the active site at the interface between the two monomers (**Figure 2**A and **Supporting Information**). As expected, the pyrophosphate moiety interacts with NH of Asp 154.B in the α_6 helix, His 65.B and His 259.B in α_{11} helix as well as with magnesium ion of the PP domain. The magnesium ion is coordinated by the carboxylate of Asp 154.B (α_6), the amide function

of Asn 184.B and carbonyl of Ile 186.B from one side and by the pyrophosphate moiety of TPP on the other side, thus stabilizing the interaction between TPP and the PP domain. A hydrophobic pocket formed by Leu 380.B, Val 408.B, Phe 433.B, Phe 436.B and Tyr 439.B of the Pyr domain and by Leu 115.A, Ile 188.A of the PP domain of the other monomer allows the binding of the pyridinium and thiazolium rings of TPP. Moreover, a hydrogen bond is formed between Glu410.B and the NH of the pyridinium ring.

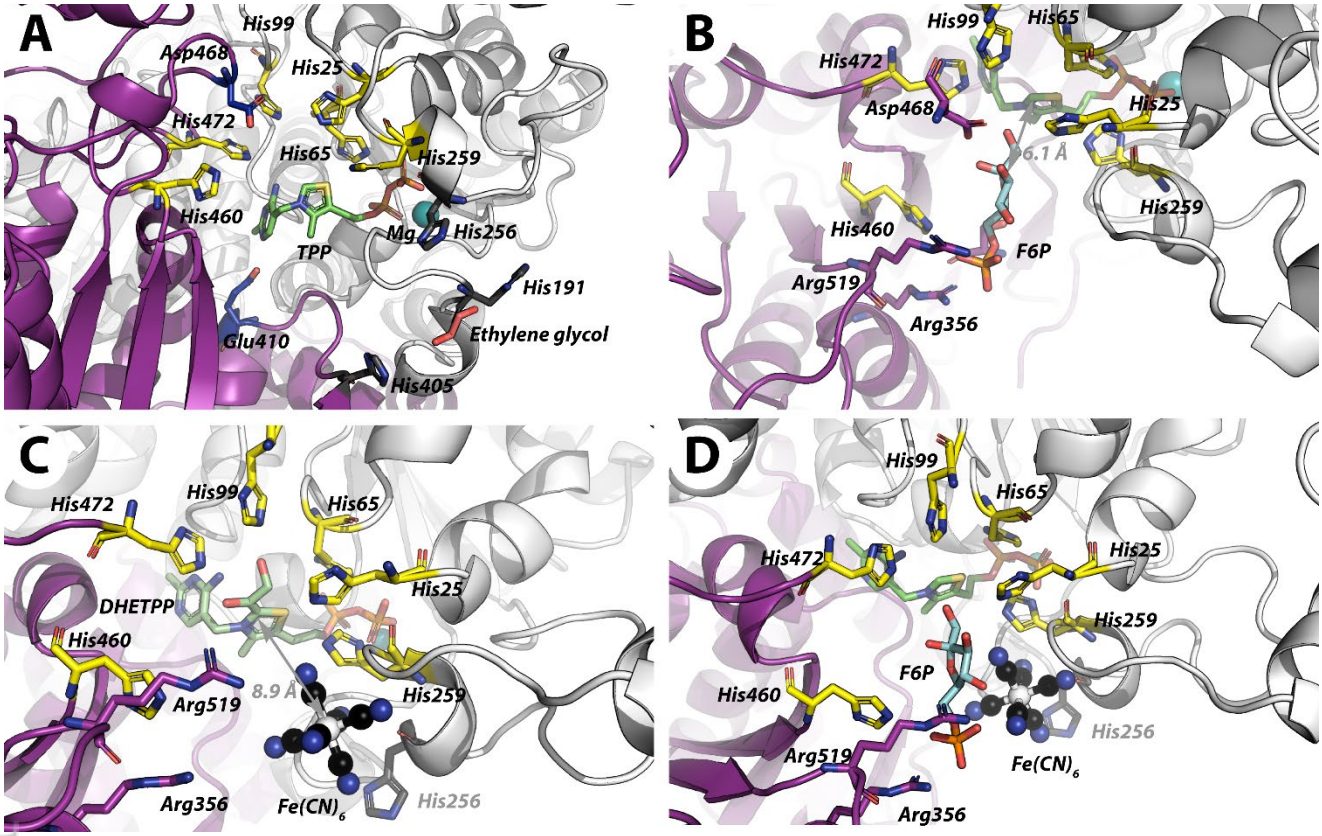

Figure 2. Histidine crown localized around the active site of *vv*TK (A). Chain A is colored in white and chain B is in purple. The histidyl residues attributed to the crown are in yellow sticks around the TPP in green. Other histidyl residues not involved in the crown and important residues (Glu 410.B, Asp 468.B) are shown in black. The magnesium ion, shown as a cyan sphere, interacts with the pyrophosphate group of TPP. A co-crystallized molecule of ethylene glycol is shown in salmon. Heteroatoms are colored as in **Figure 1**A. Docking of cyclic F6P on *vv*TK (B). F6P is shown as cyan sticks. The distance between the C2 atom of F6P and the C2 atom of the thiazolium ring of TPP is indicated as an orange arrow. Arg 356.B, Asp 468.B and Arg 519.B are shown as purple sticks. Docking of ferricyanide on *vv*TK (C). $Fe(CN)_6^{3-/4-}$ is shown as colored spheres with the iron atom in white. The distance between the iron atom of $Fe(CN)_6^{3-/4-}$ and the C2 atom of the thiazolium ring of TPP is indicated

with an orange arrow. Important residues are in stick and colored as previously described. Overlay of *vv*TK docked by F6P and $Fe(CN)_6^{3-/4-}$ (D). Residues and ligands are represented as previously described.

The C2 atom of the thiazolium ring of TPP, involved in the reaction as a carbanion, is at the bottom of a cavity but remains accessible to the solvent (**Supporting information**). This surface cavity is expected to be the substrate binding site and exhibits a crown of six histidyl residues from both monomers: His 25.A, His 65.A, His [illegible]A, His 259.A His 460.B and His 472.B.

These histidyl residues have been studied independently in the literature. His 69, His 103, His 263, and His 481 are shown to be involved in TPP stabilization [21, 59], while His 30, His 103, and His 481 are implicated in TPP activation into carbanion, as demonstrated in *sc*TK. [26] Other works focus on the stabilization of phosphorylated substrates by His 30, His 263, His 469, and His 481 in the same enzyme. [59, 60, 61] Here, we attempt to attribute each histidyl residue of the crown to one of these functions. TPP activation into the reactive carbanion (e.g. deprotonation of the C2 atom of the thiazolium ring) is still not well understood but involves hystidyl residues. As proposed by Lindqvist *et al* and Fiedler *et al* based on the *S. cerevisae* TK, [21, 26] and adapted to the *vv*TK structure, activation is probably initiated by a charge delocalization of the N1' of the pyrimidine ring of TPP by Glu 410.B leading deprotonation of the amine at the C4' position by His 472.B. The unprotonated imidazole ring readily accepts the proton from the thiazolium ring (C2 position) leading to the activated TPP (e.g. the carbanion). It is expected that protonated His 472.B is stabilized by Asp 468.B and His 99.A. It is unclear whether if His [illegible]A, His 65.A and His 259.A participate to the activation despite nitrogen atoms of His 65.A and His 259.A imidazole rings being closed to the sulfur atom of the thiazolium (<3.8 Å) and probably favoring the charge delocalization in the ring. Additionally, these two residues (His 65.A and His 259.A) stabilize the pyrophosphate moiety of TPP as a clamp together with a magnesium ion.

The importance of the other histidyl residues (His 191.A, His 256.A and His 405.B) in this region is questionable because their distance to TPP is high (>10 Å). They are located at the entrance of the substrate binding site (**Figure 2**A) and the triad formed by these three residues is in a cavity where one ethylene glycol molecule is found in the crystal. Moreover, these residues are not conserved in others TK. For example, in *S.*

cerevisae TK (PDBid: 1GPU), His 405.B is replaced by a lysyl residue (also positively charged), and His 191.A is replaced by an alanyl residue which does not appear to be relevant for substrate interaction.

Substrate docking on *vv*TK. The binding of three ligands on the *vv*TK are of importance in this: F6P as the phosphorylated ketose donor, $Fe(CN)_6^{3-}$ as oxidant of the DHETPP intermediate having a stoichiometry of two to complete the reaction (equation 1), and inhibitor I38-49 (*vide infra*). Attempts to crystallize or co-crystallize the *vv*TK with these ligands by soaking have been so far unsuccessful. In the absence of *vv*TK crystals including these ligands, docking experiments are performed.

Docking of* D-*fructose-6-phosphate. F6P is the first substrate to bind to the enzyme in the substituted (Ping-Pong) TK mechanism and is therefore used for docking. Docking is performed with both linear and cyclic (furanose) F6P (**Figure 2**B and **Supporting Information**). Only a limited number of poses (three) are obtained with linear F6P with energy not lower than -3.9 kcal.mol^{-1} and one of them do not have the ketol function properly positioned for the reaction. The other poses are located elsewhere on the *vv*TK with energies not compatible with protein-ligand interactions. Regarding the cyclic F6P, only one pose is found in the *vv*TK active site and have a free energy of - 4.58 kcal.mol^{-1}. In order to judge if this F6P pose is relevant, structures of published TK co-crystallized with substrates or products are superimposed with *vv*TK docked with F6P (**Supporting information**). In all these structures the distance between reactive carbonyl and the C2 of TPP (or TPP analogue) is comprised between 3.3 and 5.6 Å. This distance is slightly higher in the docking of F6P in *vv*TK (6.1 Å, **Figure 2**B) suggesting this pose is closed to the real F6P binding position in *vv*TK. Interactions are observed between F6P and His 460.B, His 25.B and His 472.B (<4 Å) of the histidyl crown. Additionally, His 460.B forms a hydrogen bond with an oxygen atom of the phosphate group of F6P while the guanidium moieties of Arg 356.B and Arg.519.B complete the interactions with the phosphate group of F6P (< 3Å). Finally, the last interaction with phosphate is between the hydroxyl group of Ser 383.B and the C6 oxygen atom of F6P (2.9 Å). Phosphate is shifted by ~2 Å out of the binding site compared to crystalized TK with substrates but interacts with the same arginyl residues. Interactions between the furanose ring and *vv*TK occur between the carboxylate of Asp 468.B located at less than 3.1 Å above the F6P and the C2 and C3 hydroxyl groups of F6P, between His 472.B and His 25.A with the C1 hydroxyl group of F6P and between the C4 hydroxyl and Arg 519.B. This pose seems to

corresponds to an intermediate binding of F6P prior to catalysis because the distance between the C2 atom of F6P and the C2 atom of TPP is still 6.1 Å. This docking pose probably does not correspond to the true *vv*TK-F6P complex but it highlights the importance of histidyl residues of the crown for substrate binding.

Docking of Ferricyanide. $Fe(CN)_6^{3-}$ is a metallic complex with a positively charged iron atom linked to 6 negatively charged cyanide ions, giving a net negative charge to the complex. The structures of cytoglobin from *Homo sapiens* (PDBid: 1URV, 1UT0, 1URY, 1UX9, 4B3W), bilirubin oxidase from *Myrothecium verrucaria* (PDBid: 6I3J, 6I3K) and superoxide reductase from *Desulfarculus baarsii* (PDBid: 1VZH, 1VZG) are the only ones obtained with $Fe(CN)_6^{3-}$. In all these structures, $Fe(CN)_6^{3-}$ is found at the surface of the protein and never in cavity, suggesting a relatively low affinity between these proteins and this ligand. On the other hand, $Fe(CN)_6^{3-}$ interacts strongly with homodimeric hemoglobin from *Scapharca inaequivalvis* through ionic interactions via a lysyl and arginyl cluster located 15 Å from the heme of this protein, allowing efficient electron transfer. [62]

In the case of the *vv*TK, we could expect that $Fe(CN)_6^{3-}$ binds closely to DHETPP. Another hypothesis could be that the electron transfer between DHETPP and $Fe(CN)_6^{3-}$ occurs through the histidyl crown. Several other oxidants are tried out ($Ru(bpy)_3^{2+}$, oxidized $ABTS^{+}$…) in place of $Fe(CN)_6^{3-}$ without success suggesting a selectivity of *vv*TK for $Fe(CN)_6^{3-}$ (Data not shown). In the docking experiment, the two redox forms $Fe(CN)_6^{3-}$ and $Fe(CN)_6^{4-}$ can not be distinguished as far as we know and they are refered as $Fe(CN)_6^{3-/4-}$ in this section to avoid confusion.The docking of $Fe(CN)_6^{3-/4-}$ on *vv*TK is done with enzyme containing DHETPP or TPP (**Figure 2**C) . In both case a unique pose is obtained. Despite the required stoichiometry of two $Fe(CN)_6^{3-}$ molecules for the oxidation of one DHETPP, only one $Fe(CN)_6^{3-}$ could be docked. $Fe(CN)_6^{3-/4-}$ is found close to the nitrogen atoms of imidazole rings of His 25.A, His 259.A (both in the histidyl crown, at 4.1 Å and 3.7 Å, respectively) and in the proximity of His 256.A (4.5-4.7 Å). These distances are reported on **Table 3**. One cyanide moiety could also be stabilized by the hydroxyl group of Ser 383.B and nitrogen atom of Pro 382.B located at 2.7 and 4.1 Å, respectively (not shown for clarity). In this pose, the $Fe(CN)_6^{3-/4-}$ iron atom is located at 8.7 Å from the C2 of the thiazolium ring of the DHETPP. According to the Marcus equation, [63, 64] $Fe(CN)_6^{3-/4-}$ is at the optimal distance of DHETPP between 5 Å and 15 Å. His 25.A and His 259.A could also participate in the electron transfer acting as electron relays. This suggests that $Fe(CN)_6^{3-}$ should be considered as a Michaelian substrate for *vv*TK and

mechanism elucidation should include the existence of a $Fe(CN)_6^{3-}$-*vv*TK complex. It should be noted that some of the TK co-crystallized with their substrates are also assayed using $Fe(CN)_6^{3-}$ but the $Fe(CN)_6^{3-}$-TK complexes are not investigated (**Supporting Information**).

Table 2. Residues involved in the interaction with $Fe(CN)_6^{3-/4-}$.

Residue	atom	*vv*TK-TPP complex	*vv*TK-DHETPP complex
His 25.B	NE2	6.2 Å	4.1 Å
His 256.B	N	2.9 Å	4.5 Å
His 259.B	N	4.5 Å	3.7 Å
TPP or DHETPP	C2	10.3 Å	8.7 Å
ΔG° (kcal/mol)		-4.51	-5.43

Distance is determined between the atom of the residue and closest nitrogen atom of $Fe(CN)_6^{3-}$ except for TPP and DHETPP where it is determined using the iron atom. Free energies of dockings and K_D are calculated using AMDock.

When the docking is done with *vv*TK containing TPP instead of DHETPP, only few differences are observed regarding involved residues (**Table 3**). Nevertheless, $Fe(CN)_6^{3-/4-}$ is found closer to His 256.A and consequently further from His 25.A, His 259.A and from the C2 atom of TPP. This suggests that $Fe(CN)_6^{3-/4-}$ could also bind *vv*TK containing TPP. Regarding the charge and the size of $Fe(CN)_6^{3-/4-}$, this would be a potential competitor of F6P binding or of another $Fe(CN)_6^{3-/4-}$ molecules. Unfortunately, it was impossible to determine by docking experiments how a second $Fe(CN)_6^{3-/4-}$ could interact within an existing *vv*TK-DHETPP-$Fe(CN)_6^{3-/4-}$ complex because the algorithm erases the first docked $Fe(CN)_6^{3-/4-}$ molecule. The second $Fe(CN)_6^{3-/4-}$ could be considered henceforth as a substrate with a binding site affording a *vv*TK-(DHE)TPP-$(Fe(CN)_6^{3-/4-})_2$ complex or simply as a chemical oxidant for the first bound $Fe(CN)_6^{3-/4-}$. This remains to be elucidated.

Finally, the possibility for the *vv*TK to simultaneously bind F6P and $Fe(CN)_6^{3-/4-}$ is investigated (**Figure 2**D). The superposition of the docking poses for each substrate do not evidence any steric clashes. The closest distance between C4 hydroxyl of F6P and the closest nitrogen atom of $Fe(CN)_6^{3-/4-}$ is 3.9 Å. Considering the radius of these atoms,[65] these molecules are 1.05 Å apart, but additional local movements in the *vv*TK in solution can allow or disallow the concomitant binding of F6P and $Fe(CN)_6^{3-/4-}$. In the transferase reaction, TKs follow a substituted mechanism (ping-pong) with successive binding of the ketose donor and aldose acceptor. In the present case, the

possibility for both F6P and $Fe(CN)_6^{3-}$ to bind simultaneously on the enzyme could also lead to a sequential (ordered or non-ordered) mechanism (*vide infra*). In addition to the current work performed on *vv*TK, these results could be probably extrapolated to other TKs considering the structural homology between these enzymes.

Docking of I38-41, an inhibitor of ecTK. In a previous study, I38-49 is shown to inhibit the *ec*TK following a partial mixed mechanism when TPP concentration varies. The assay is conducted using L-erythrulose as ketose substrate together with $Fe(CN)_6^{3-}$ as oxidant. [37] I38-49 is also an inhibitor of *vv*TK (*vide infra*). In the absence of crystallographic information regarding the specific interaction between I38-49 and *vv*TK, we performed docking experiments in order to identify putative binding sites and to contribute to elucidate the inhibition mechanism (**Figure 3**, **Table 4**, **Supporting information**).

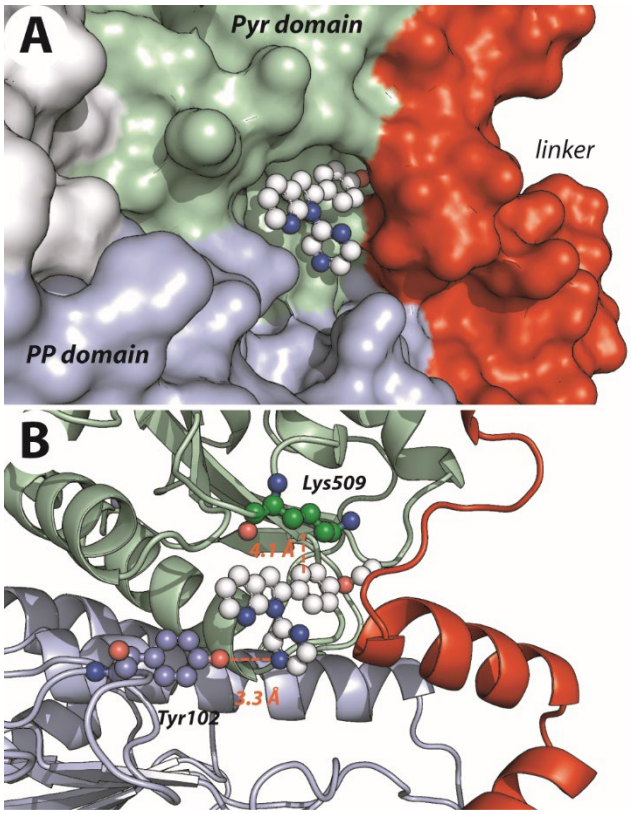

Figure 3: Best pose of I38-49 docked on *vv*TK shown as surface (A) and ribbons (B). The domains are colored according to **Figure 1**B (PP domain in blue, Pyr domain in green, linker between the two domains in red). I38-49 is shown as balls and sticks with carbon atoms in white, nitrogen in blue and oxygen in red. Residues Tyr102 and Lys509 are shown as ball and sticks with carbon atoms colored according to the *vv*TK domain. Distances between these residues and I38-49 are shown as orange dotted lines.

Ten poses are proposed after docking I38-49 on the *vv*TK structure filled with TPP. The first four poses, corresponding to the more stable complexes, are found in the same cavity located at the interface between PP domain, Pyr domain and first linker (**Figure 3**, **Supporting information**). This cavity is formed by loops between helix α_2 and sheet β_1 and helices α_4 and α_5 of the PP domain, between helix α_{19} and sheet β_8, helix α_{21} and sheet β_9 and helix α_{21} and sheet β_9 of the Pyr domain and by the loop between helices α_{15} and α_{16} of the first linker (**Figure 3**). In particular, the loop between helices α_4 and α_5 (29-residues long) must be flexible enough to accept ligands and/or to induce movements inside the PP domain and further cooperative behavior. Residues 326-329 of the first linker and Tyr102 of the PP domain complete the closure of the cavity. Several orientations of I38-49 in this cavity are obtained but always with the 7-aza-indole and the phenyl rings in the same plane (**Supporting information**). Only the fifth pose of I38-49 is positioned at the entry of the active site, the phenyl ring occupying the position of the F6P cycle and the indole ring being at 4-5 Å of the guanidinium moiety of Arg519. The last four poses show non-relevant interactions with the surface of the PP domain (pose #6), with the TEV protease cleavage site (pose #7) or with the C-ter domain (poses #8 and #9). The tenth pose shows I38-49 positioned on the other side of the linker compared to poses #1-4, also with possible interactions between the Oxygen O_{7c} with Asn 402 and N_{7a}.

According to the free energy (-9.98 to -11.20 kcal.mol^{-1}, **Table 4**), no position could be definitively excluded but the number of poses in the cavity of the Pyr domain seems to indicate a preferential position. In this case, as I38-49 is found close to the crossroad of Pyr domain, PP domain and first linker, domain movement suspected to lead to cooperativity (*vide infra*).

Table 3. Free energies of I38-49 docked on *vv*TK-TPP.

Ranking	Free energy (kcal.mol^{-1})
1	-11.20
2	-11.14
3	-10.97
4	-10.85
5	-10.17

6	-9.98
7	-9.60
8	-9.11
9	-9.11
10	-9.04

Enzyme kinetics. The assay proposed by Kochetov *et al.* [35] is used to measure *vv*TK activity, based on the oxidation of the DHETPP intermediate by two molecules of $Fe(CN)_6^{3-}$ (λ_{max} = 420 nm, yellow) together with one water molecule yielding two uncolored $Fe(CN)_6^{4-}$ molecules (equation 1). In the present work, F6P is used as ketose because the furanose configuration protect the ketone function from oxidation by $Fe(CN)_6^{3-}$, as opposed to other available TK ketones substrates (e.g. β-hydroxypyruvate or L-erythrulose).

The exact mechanism of the reaction involving $Fe(CN)_6^{3-}$ is still not well understood probably because of its complexity : two $Fe(CN)_6^{3-}$ molecules are involved, one water molecule is necessary to respect the mass balance and the two carbons units are released as glyoxylate with unknown reaction sequence. It is nevertheless accepted that the first reaction step leads to DHETPP and to the release of E4P. Then, two ferricyanide molecules oxidize DHETPP back into TPP with a water molecule forming one molecule of glyoxylate (equation 1). This second step is irreversible. Therefore, taking the advantage of having access to *vv*TK, we investigate its steady-state kinetics.

Rate vs TPP. Reaction rates (v_0) are determined under F6P (0.5 mM) and $Fe(CN)_6^{3-}$ (1 mM) while TPP concentration varied **(Supporting Information)**. In this case, the *vv*TK follows a Michaelian behavior (confirmed by the Hanes-Wolf plot) with an apparent K_M^{TPP} of 2.62 ± 0.20 µM, an apparent V_m value of 11.36 ± 0.27 µM.min^{-1} (k_{cat} of 0.21 ± 0.01 s^{-1}). The K_M value is similar to the one of the *ec*TK (1.8-4.8 µM) and close to the one of eukaryotes (0.6 µM for *sc*TK, 7 µM for *Mus musculus* TK and 0.4 µM for *Homo sapiens* TK).

Rate vs F6P and $Fe(CN)_6^{3-}$. The reaction rate is then evaluated as the function of [F6P] (0-500 µM) and [$Fe(CN)_6^{3-}$] (0-2000 µM)(**Figure 4**). When one of the substrate concentration is constant, the rate increases with the concentration of the other substrate according to an apparent Michaelis-Menten mechanism. Therefore, F6P interacts with *vv*TK forming a TK-F6P complex as expected. $Fe(CN)_6^{3-}$ also forms a reversible complex with

*vv*TK as already suggested by the docking experiments and now confirmed by the kinetic study. At this stage, it is still impossible to determine how the two $Fe(CN)_6^{3-}$ molecules interact with *vv*TK, e.g. if they bind simultaneously or one after the other. The Lineweaver-Burk plots clearly exhibit bundles of unparallel straight lines with an intersection point far from the *y*-axis ($1/v_0$ axis) (**Figure 4**). This could correspond to several mechanism such as steady-state ordered, Theorell-Chance or random kinetic mechanisms. In this assay both F6P and $Fe(CN)_6^{3-}$ should bind to *vv*TK before the release of the product. This excludes the substituted mechanism observed when TK catalyzes the transferase reaction. When F6P concentrations varies, the Michaelis-Menten plot sometimes shows a slight sigmoidal shape suggesting some cooperativity of the *vv*TK for F6P. Hill coefficients [illegible] not convincing regarding the low fitting quality and/or *h* indices below 1.2 (Data not shown). Kochtetov *et al.* also suggest that some cooperativity could exist in TK but without clear evidence. [61, 66]

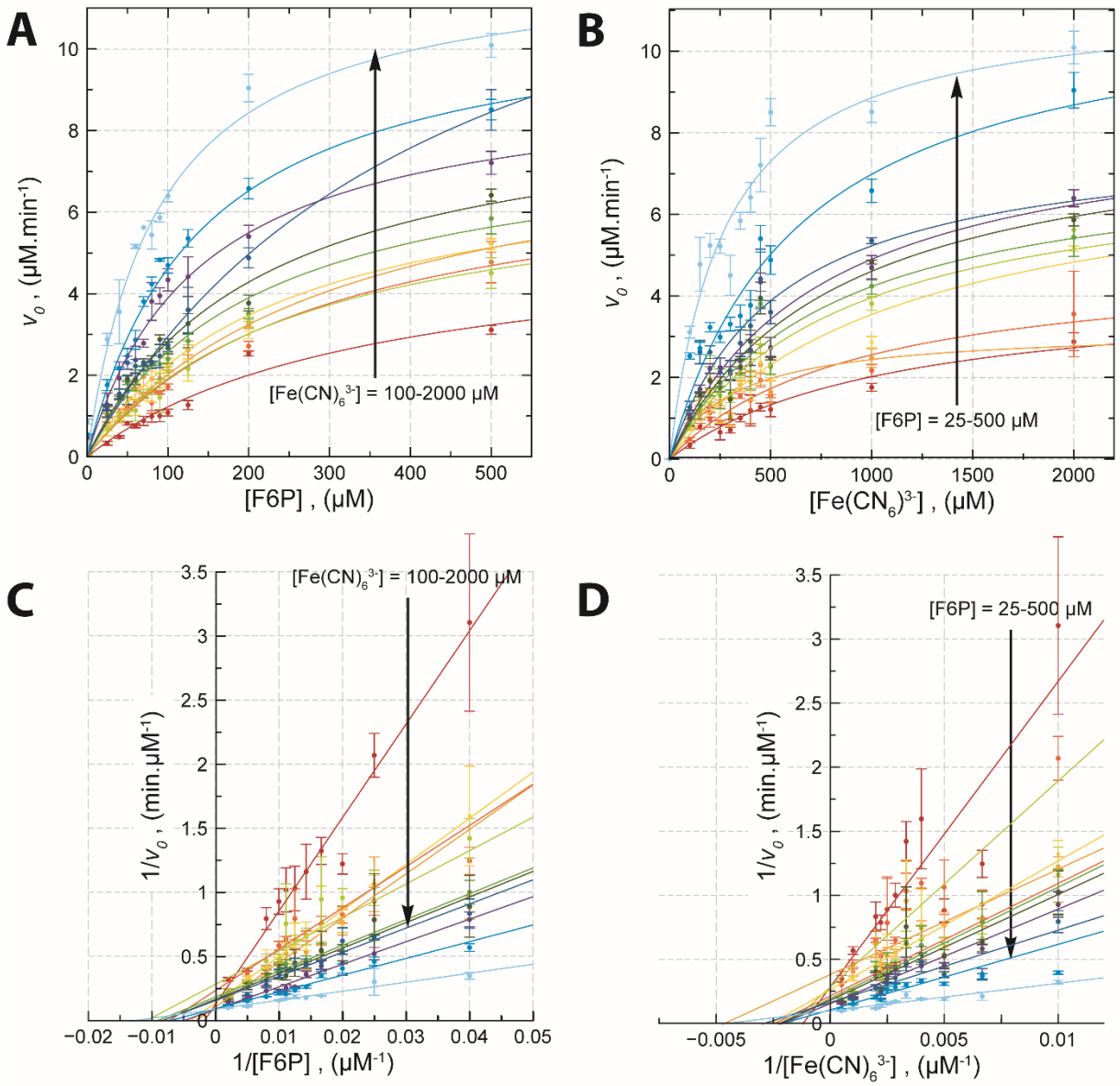

Figure 4: Michaelis-Menten (A, B) and Lineweaver-Burk plots of *vv*TK activity with varying [F6P] (A, C) or [$Fe(CN)_6^{3-}$] (B, D), the other substrate concentration being constant. All reactions are performed using 0.9 µM *vv*TK in 50 mM Hepes buffer pH 7.0, 100 mM KCl, 2 mM $MgCl_2$, 200 µM TPP at 37 °C. F6P concentrations are 25. 40, 50, 60, 70, 80, 90, 100, 125, 200 and 500 µM and $Fe(CN)_6^{3-}$ concentrations were 100, 150, 200, 250, 300, 350, 400, 450, 500, 1000 and 2000 µM (n =3). Attempts to identify the mechanism by model discrimination using enzyme kinetic software (e.g. Dynafit) [67] or by classical analysis is yet unsuccessful without product inhibition studies.

The apparent V_m values obtained from Michaelis-Menten and Lineweaver-Burk plots (V_m^{app}) are used to obtain the secondary plots $V_m^{app} = f([Fe(CN)_6^{3-}])$ and $V_m^{app} = f([F6P])$ corresponding to the Michaelis-Menten plots

when the other substrate is saturating. This allows to determine the K_M values for both substrates (K_{F6P}^{app} = 66 ± 18 µM and K_{FeCN6}^{app} = 139 ± 28 µM) and V_m values (12.34 ± 0.71 to 13.60 ± 1.45 µM.min^{-1}) (**Supporting information**). This is the first determination of K_{FeCN6} for a TK. For comparison, apparent K_{F6P} is found to be 600 µM for *mt*TK [19] and 340 µM for *hs*TK [68], using the same assay, probably because these values are determined under non saturating $Fe(CN)_6^{3-}$ concentrations (0.5 mM and 1.25 mM, respectively).

When DHETPP is oxidized, two electrons have to transferred to $Fe(CN)_6^{3-}$ but only one molecule can bind to the *vv*TK active site according to the docking experiment. We strongly believe that one of the electrons could be transiently accepted by the histidyl residues of the crown, the other being accepted by $Fe(CN)_6^{3-}$. After release of the first $Fe(CN)_6^{4-}$ (reduced), a second $Fe(CN)_6^{3-}$ could bind to accept the second electron. Alternatively, a radical product could be released and oxidized into glyoxylate outside of the enzyme active site by free $Fe(CN)_6^{3-}$ molecules. This contribution to the deciphering TK-catalysed reaction using the $Fe(CN)_6^{3-}$ assay highlights the probable role of the histidyl crown, the existence of TK-F6P-$Fe(CN)_6^{3-}$ ternary complex and the fact that this simple and easy-to-handle assay requires much more effort to be fully understood.

Inhibition by I38-49. The I38-49 inhibitor is evaluated on *vv*TK against F6P binding (**Figure 5**). In the absence of I38-49, *vv*TK adopts a non-cooperative behavior with kinetic parameters similar to those observed previously (V_m^{app} = 8.70 ± 0.41 µM. min^{-1}, K_{F6P} = 106 ± 7 µM). As the concentration of I38-49 increases from 25 to 400 µM, reaction rates decrease and *vv*TK adopted a cooperative behaviour as shown by the sigmoidal shape of the curves. This indicates that the binding of I38-49 induces conformational changes on *vv*TK with an inhibition constant K_{I38-49} (e.g. K_i in usual kinetic models). Data are fitted using the Hill equation allowing the apparent V_m, $K_{0.5}$ and *h* values to be determined for each I38-49 concentration.

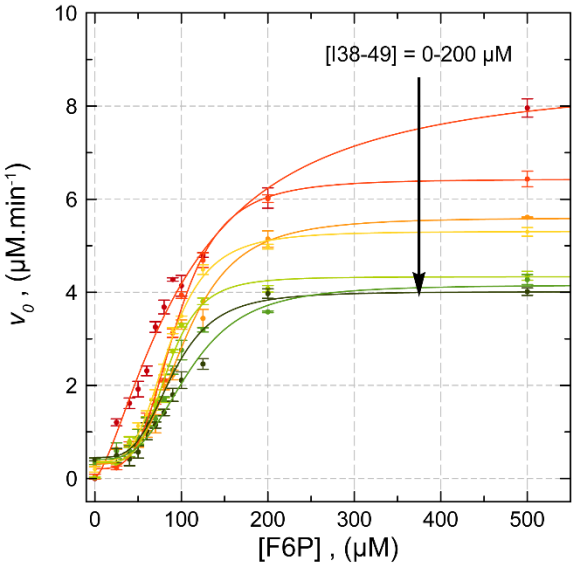

Figure 5: Cooperativity of *vv*TK vs F6P induced by I38-49. Reactions are performed using 0.9 µM *vv*TK in 50 mM Hepes buffer pH 7.0, 100 mM KCl, 2 mM $MgCl_2$, 200 µM TPP, 1 mM $Fe(CN)_6^{3-}$ at 37 °C. I38-49 concentrations are 0, 25, 50, 75, 100, 200 and 400 µM (n =3).

At saturating [F6P], the V_m^{app} value decreases with [I38-49] meaning that I38-49 is not a competitor of F6P and binds to another site, that could be the one suggested by the docking experiment (**Figure 3**). At these high [F6P], V_m^{app} value decreases following a non-cooperative binding (e.g. hyperbolic) with a K_{I38-49} value of 30.71 ± 7.58 µM. Interestingly, at saturating [I38-49], around 35% of the *vv*TK activity is still observed (partial inhibition of *vv*TK). This was previously observed for this inhibitor with *ec*TK. [37] This could be explained in two ways: I38-49 binds on both *vv*TK monomers and induces conformational changes that decrease the k_{cat} value of both monomers ([F6P] and $[Fe(CN)_6^{3-}]$ are in excess in this case), or I38-49 binds to one monomer and induces conformational changes inhibiting one monomer and preventing the binding of another I38-49 molecule on the other monomer, leaving the second active site ready for catalysis.

The $K_{0.5}$ value ([F6P] for a rate equal to half the maximum rate) is not significantly affected by the presence of I38-49 meaning its binding does not affects the binding of F6P, considering that $K_{0.5}$ approximates individual F6P dissociation constants (**Supporting information**). This confirms the non-competitive binding of I38-49. Finally, the Hill coefficient, close to 1 in the absence of I38-49, drastically increases to 3.3-4.4 in the presence of I38-49

(**Supporting information**). This states that, once I38-49 is bound, *vv*TK adopted a cooperative behaviour regarding F6P binding.

We could hypothesize that, in the presence of I38-49, F6P binds to one of *vv*TK active site but is not transformed even at low concentrations considering the non-competitive nature of I38-49. At [F6P] above $K_{0.5}$ value, the second active site could be occupied, probably leading to another *vv*TK conformation and activity is partially recovered.

I38-49 was previously shown to inhibit *ec*TK (K_i value of 3.4 µM versus TPP binding) when activity is measured with saturating *L*-ery and $Fe(CN)_6^{3-}$ concentrations. [37] Similarly, V_m^{app} value decreases as I38-49 concentration increases but *ec*TK cannot be fully inactivated suggesting that one *ec*TK active site is still available for catalysis similarly to *vv*TK. This can only be explained by conformational changes in the *ec*TK induced by I38-49. Moreover, as the varying substrate was TPP, no cooperativity was observed but should be evaluated in the near future.

Discussion (Conclusion)

We have solved the structure of a new TK from *Vibrio vulnificus*, a Human pathogen organism whose expansion zone could grow in the future, which justifies increased knowledge and monitoring. The *vv*TK structure is similar to previously described TK,with a small difference in the first linker between the PP and Pyr domains formed by four helices instead of two on other TK (**Figure 1**). We also highlight the existence of a crown formed by 6 histidyl residues around the TPP binding site (**Figure 2**A). Its role, if any, has to be clarified but it is probably involved in the TPP activation into carbanion. To assess activity, the oxidation rate of the DHETPP by $Fe(CN)_6^{3-}$ is used with F6P as the donor substrate.[35] In the absence of other crystallographic structures, docking of cyclic F6P and $Fe(CN)_6^{3-/4-}$ suggest that both substrates could bind simultaneously to *vv*TK (**Figure 2**). This raises the question of the enzyme mechanism using $Fe(CN)_6^{3-}$. The natural transferase reaction catalyzed by TK follows a substituted mechanism (Ping-Pong) but the docking experiments suggest that, using $Fe(CN)_6^{3-/4-}$, a sequential mechanism is also possible. This is confirmed by steady-state kinetics with K_{F6P}^{app} = 66 ± 18 µM and K_{FeCN6}^{app} = 139 ± 28 µM) (**Figure 4**). In fact, this is the first kinetic study of the oxidation of DHETPP by $Fe(CN)_6^{3-/4-}$ in a TK catalyzed reaction, as far as we know and the first evidence of the existence of a *vv*TK-$Fe(CN)_6^{3-/4-}$ complex. Obviously, this is only a partial elucidation of the mechanism but it is highly intriguing and would deserve much more effort to be fully understood in the future, requiring access to the kinetic release of E4P and glyoxylate, isotopic studies to understand to role of the water molecule, as well EPR experiments to study DHETPP oxidation by $Fe(CN)_6^{3-}$.

Compound I38-49 discovered to inhibit *ec*TK is also active on *vv*TK with an unexpected mechanism. I38-49 induces a cooperative behaviour regarding F6P binding (**Figure 5**).[37] Cooperativity of TK was suggested in the literature but never formerly demonstrated. It is evidenced here for the first time, thanks to I38-49. However, I38-49 does not lead to full TK inhibition meaning that the second binding site is modified by binding to the first one, probably locking one monomer in an active conformation. As co-crystallisation of *vv*TK with I38-49 is yet unsuccessful, docking is done suggesting a binding site at the interface between the PP and Pyr domains and the linker between them (**Figure 3**). This putative site was never described for any other TK and could be a new

target for drugs or metabolites in the PPP regulation. In the future, it should be more deeply investigated in *vv*TK but also in other TK to enable the design specific drugs.

AUTHOR INFORMATION

Corresponding Author

* Bastien Doumèche ; Email: doumeche@univ-lyon1.fr

* Franck Charmantray ; franck.charmantray@uca.fr

Author Contributions

The manuscript was written through contributions of all authors. All authors have given approval to the final version of the manuscript. ‡These authors contributed equally.

Funding Sources

The Project CEITOP (*Criblage Electrochimique d'Inhibiteur de Transcétolases d'Organismes Pathogènes*) is funded by the Region Auvergne-Rhone-Alpes (AuRA).

ACKNOWLEDGMENT

The AuRA region is greatly acknowledged for the funding of one of us (R.-N. G.). The authors thank the European Synchrotron Radiation Facility for access to MX-beamlines. Technical support from all the beamlines staff is gratefully acknowledged.

REFERENCES

1. Hsueh PR, Lin CY, Tang HJ, Lee HC, Liu JW, Liu YC, Chuang YC (2004) *Vibrio vulnificus* in Taiwan. *Emerging Infectious Diseases*, *10*:1363–1368.
2. Baker-Austin C, Oliver JD (2020) Vibrio vulnificus. *Trends in Microbiology*, *28*:81–82.
3. Phillips KE, Satchell KJF (2017) Vibrio vulnificus: From oyster colonist to Human pathogen. *PLOS Pathogens*, *13*:e1006053.
4. Doktor K, Fraimow H (2020) *Vibrio vulnificus* infections from a previously nonendemic area. *Annals of Internal Medicine*, *172*:367.
5. Baker-Austin C, Oliver JD (2018) *Vibrio vulnificus*: New insights into a deadly opportunistic pathogen: *Vibrio vulnificus* review. *Environmental Microbiology*, *20*:423–430.
6. Trinanes J, Martinez-Urtaza J (2021) Future scenarios of risk of Vibrio infections in a warming planet: A global mapping study. *The Lancet Planetary Health*, *5*:e426–e435.
7. Farmer JJ (1979) Vibrio ("Beneckea") vulnificus, the bacterium associated with sepsis, scepticaemia, and the sea. *The Lancet*, *314*:903.
8. Hori M, Nakayama A, Kitagawa D, Fukushima H, Asai H, Kawai Y, Okuchi K (2017) A case of Vibrio vulnificus infection complicated with fulminant purpura: Gene and biotype analysis of the pathogen. *JMM Case Reports*, *4*.
9. Park J, Lee CS (2018) *Vibrio vulnificus* Infection. *New England Journal of Medicine*, *379*:375–375.
10. Tan X, Ramond E, Jamet A, Barnier JP, Decaux-Tramoni B, Dupuis M, Coureuil M. (2019) Transketolase of Staphylococcus aureus in the control of master regulators of stress response during infection. *The Journal of Infectious Diseases*, *220*:1967–1976.
11. Horecker BL, Gibbs M, Klenow H, Smyrniotis PZ (1954) The mechanism of pentose phosphate conversion to hexose monophosphate. I. With a liver enzyme preparation. *The Journal of Biological Chemistry*, *207*:393–403.

12. Gibbs M, Horecker BL (1954) The mechanism of pentose phosphate conversion to hexose monophosphate. II. With pea leaf and pea root preparations. *The Journal of Biological Chemistry*, *208:*813–820.
13. Schenk G, Duggleby RG, Nixon PF (1998) Properties and functions of the thiamin diphosphate dependent enzyme transketolase. *The International Journal of Biochemistry & Cell Biology*, *30*:1297–1318.
14. Bozdech Z, Ginsburg H (2005) Data mining of the transcriptome of Plasmodium falciparum: The pentose phosphate pathway and ancillary processes. *Malaria Journal*, *4*:17.
15. Cascante M, Centelles J J, Veech RL, Lee WNP, Boros LG (2000) Role of Thiamin (Vitamin B-1) and Transketolase in tumor cell proliferation. *Nutrition and Cancer*, *36*:150–154.
16. Boros LG, Puigjaner J, Cascante M, Lee WN, Brandes JL, Bassilian S, Schirmer WJ (1997) Oxythiamine and dehydroepiandrosterone inhibit the nonoxidative synthesis of ribose and tumor cell proliferation. *Cancer Research*, *57*:4242–4248.
17. Joshi S, Singh AR, Kumar A, Misra PC, Siddiqi MI, Saxena JK (2008) Molecular cloning and characterization of Plasmodium falciparum transketolase. *Molecular and biochemical parasitology*, 160(1), 32–41.
18. Hasan MA, Mazumder MH, Chowdhury AS, Datta A, Khan MA (2015) Molecular-docking study of malaria drug target enzyme transketolase in Plasmodium falciparum 3D7 portends the novel approach to its treatment. *Source code for biology and medicine*, 10, 7.
19. Fullam E, Pojer F, Bergfors T, Jones TA, Cole ST (2012) Structure and function of the transketolase from *Mycobacterium tuberculosis* and comparison with the human enzyme. *Open Biology*, *2*:110026
20. Rabe von Pappenheim F, Aldeghi M, Shome B, Begley T, de Groot BL, Tittmann K (2020) Structural basis for antibiotic action of the B1 antivitamin 2'-methoxy-thiamine. *Nature chemical biology*, 16(11), 1237–1245.
21. Fiedler E, Thorell S, Sandalova T, Golbik R, König S, Schneider G (2002) Snapshot of a key intermediate in enzymatic thiamin catalysis: Crystal structure of the α-carbanion of (α,β-dihydroxyethyl)-thiamin

diphosphate in the active site of transketolase from *Saccharomyces cerevisiae*. *Proceedings of the National Academy of Sciences*, *99*:591–595.

22. Muller YA, Lindqvist Y, Furey W, Schulz GE, Jordan F, Schneider G (1993) A thiamin diphosphate binding fold revealed by comparison of the crystal structures of transketolase, pyruvate oxidase and pyruvate decarboxylase. *Structure*, *1*:95–103.
23. Mitschke L, Parthier C, Schröder-Tittmann K, Coy J, Lüdtke S, Tittmann, K (2010) The crystal structure of Human transketolase and new Insights into its mode of action. *Journal of Biological Chemistry*, *285*:31559–31570.
24. Kochetov GK, Philippov PP (1970) The function of calcium—Cofactor of transketolase from baker's yeast. *FEBS Letters*, *6*:49–51.
25. Muller YA, Schulz GE (1993) Structure of the thiamine- and flavin-dependent enzyme pyruvate oxidase. *Science*, *259*:965–967.
26. Lindqvist Y, Schneider G, Ermler U, Sundström M (1992) Three-dimensional structure of transketolase, a thiamine diphosphate dependent enzyme, at 2.5 A resolution. *The EMBO Journal*, *11*:2373–2379.
27. Rask-Andersen M, Almén MS, Schiöth HB (2011) Trends in the exploitation of novel drug targets. *Nature Reviews Drug Discovery*, *10*:579–590.
28. Li YH, Yu CY, Li XX, Zhang P, Tang J, Yang Q, Zhu F (2018) Therapeutic target database update 2018: Enriched resource for facilitating bench-to-clinic research of targeted therapeutics. *Nucleic Acids Research*, *46*:D1121–D1127.
29. Debouck C, Metcalf B (2000) The impact of genomics on drug discovery. *Annual Review of Pharmacology and Toxicology*, *40*:193–208.
30. Šali A (1998) 100,000 protein structures for the biologist. *Nature Structural Biology*, *5*:1029–1032.
31. Dove A (1999) Proteomics: Translating genomics into products? *Nature Biotechnology*, *17*:233–236.
32. Sevostyanova IA, Solovjeva ON, Kochetov GA (2006) Two methods for determination of transketolase activity. *Biochemistry (Moscow)*, *71*:560–562.

33. Bykova IA, Solovjeva ON, Meshalkina LE, Kovina MV, Kochetov GA (2001) One-Substrate Transketolase-Catalyzed Reaction. *Biochemical and Biophysical Research Communications*, *280*:845–847.

34. Hecquet L, Bolte J, Demuynck C (1993) New assays for transketolase. *Bioscience, Biotechnology, and Biochemistry*, *57*:2174–2176.

35. Kochetov GA (1982). Determination of transketolase activity via ferricyanide reduction. In *Methods in Enzymology,* 89:43-44 (Vol. 89, pp. 43–44). Elsevier.

36. Aymard C, Bonaventura C, Henkens R, Mousty C, Hecquet L, Charmantray F, Doumèche B (2017) High-throughput electrochemical screening assay for free and immobilized oxidases: Electrochemiluminescence and intermittent pulse amperometry. *ChemElectroChem*, *4*:957–966.

37. Aymard CMG, Halma M, Comte A, Mousty C, Prévot V, Hecquet L, Doumèche B (2018) Innovative electrochemical screening allows transketolase inhibitors to be identified. *Analytical Chemistry*, *90*:9241–9248.

38. Touisni N, Charmantray F, Hélaine V, Hecquet L, Mousty C (2014) An efficient amperometric transketolase assay: Towards inhibitor screening. *Biosensors and Bioelectronics*, *62*:90–96.

39. Nam H, Hwang BJ, Choi D, Shin S, Choi M (2020) Tobacco etch virus (TEV) protease with multiple mutations to improve solubility and reduce self-cleavage exhibits enhanced enzymatic activity. *FEBS Open Bio*, *10*:619–626.

40. Datta AG, Racker E (1961) Mechanism of action of transketolase. I. Properties of the crystalline yeast enzyme. *The Journal of Biological Chemistry*, *236*:617–623.

41. De La Haba G, Leder IG, Racker E (1955) Crystalline transketolase from bakers' yeast: Isolation and properties. *The Journal of Biological Chemistry*, *214*:409–426.

42. Le Cann F, Delehouzé C, Leverrier-Penna S, Filliol A, Comte A, Delalande O, Dimanche-Boitrel MT (2017) Sibiriline, a new small chemical inhibitor of receptor-interacting protein kinase 1, prevents immune-dependent hepatitis. *The FEBS Journal*, *284*:3050–3068.

43. Waterhouse A, Bertoni M, Bienert S, Studer G, Tauriello G, Gumienny R, Schwede T (2018) SWISS-MODEL: Homology modelling of protein structures and complexes. *Nucleic Acids Research*, *46*:W296–W303.

44. Studer G, Rempfer C, Waterhouse A M, Gumienny R, Haas J, Schwede T (2020). QMEANDisCo—Distance constraints applied on model quality estimation. *Bioinformatics*, *36*:1765–1771.

45. Richardson JS, Williams CJ, Hintze BJ, Chen VB, Prisant MG, Videau LL, Richardson DC (2018). Model validation: Local diagnosis, correction and when to quit. *Acta Crystallographica Section D Structural Biology*, *74*:132–142.

46. Chen VB, Arendall WB, Headd JJ, Keedy DA, Immormino RM, Kapral GJ, Richardson DC (2010) *MolProbity*: All-atom structure validation for macromolecular crystallography. *Acta Crystallographica Section D Biological Crystallography*, *66*:12–21.

47. Guex N, Peitsch MC (1997). SWISS-MODEL and the Swiss-Pdb viewer: An environment for comparative protein modeling. *Electrophoresis*, *18*:2714–2723.

48. Laskowski RA, MacArthur MW, Moss DS, Thornton JM (1993) PROCHECK: A program to check the stereochemical quality of protein structures. *Journal of Applied Crystallography*, *26*:283–291.

49. Bowie JU, Lüthy R, Eisenberg D (1991) A method to identify protein sequences that fold into a known three-dimensional structure. *Science*, *253*:164–170.

50. Colovos C, Yeates TO (1993) Verification of protein structures: Patterns of nonbonded atomic interactions. *Protein Science*, *2*:1511–1519.

51. Wilkins M R, Gasteiger E, Bairoch A, Sanchez JC, Williams KL, Appel RD, Hochstrasser DF (1998) Protein identification and analysis tools in the ExPASy server. In A. J. Link, *2-D Proteome Analysis Protocols*, 112:531–552. New Jersey: Humana Press.

52. Kabsch W (2010) XDS. *Acta Crystallographica Section D Biological Crystallography*, *66*:125–132.

53. Afonine PV, Mustyakimov M, Grosse-Kunstleve RW, Moriarty NW, Langan P, Adams PD (2010) Joint X-ray and neutron refinement with phenix.refine. *Acta Crystallographica Section D Biological Crystallography*, *66*:1153–1163.

54. Emsley P, Lohkamp B, Scott WG, Cowtan K (2010) Features and development of Coot. *Acta Crystallographica Section D Biological Crystallography*, *66*:486–501.

55. Emsley P, Cowtan, K (2004) Coot: Model-building tools for molecular graphics. *Acta Crystallographica Section D Biological Crystallography*, *60*:2126–2132.

56. Liebschner D, Afonine PV, Baker ML, Bunkóczi G, Chen VB, Croll TI, Adams PD (2019) Macromolecular structure determination using X-rays, neutrons and electrons: Recent developments in *Phenix*. *Acta Crystallographica Section D Structural Biology*, *75*:861–877.

57. O'Boyle NM, Banck M, James CA, Morley C, Vandermeersch T, Hutchison GR (2011) Open Babel: An open chemical toolbox. *Journal of Cheminformatics*, *3*:33.

58. Valdés-Tresanco MS, Valdés-Tresanco ME, Valiente PA, Moreno E (2020) AMDock: A versatile graphical tool for assisting molecular docking with Autodock Vina and Autodock4. *Biology Direct*, *15*:12.

59. Robinson BH, Chun K (1993) The relationships between transketolase, yeast pyruvate decarboxylase and pyruvate dehydrogenase of the pyruvate dehydrogenase complex. *FEBS letters*, 328(1-2), 99–102.

60. Nilsson U, Meshalkina L, Lindqvist Y, Schneider G (1997) Examination of substrate binding in thiamin diphosphate-dependent transketolase by protein crystallography and site-directed mutagenesis. *The Journal of biological chemistry,* 272(3), 1864–1869.

61. Kochetov GA, Solovjeva ON (2014) Structure and functioning mechanism of transketolase. *Biochimica et biophysica acta*, 1844(9), 1608–1618.

62. Colotti G, Verzili D, Boffi A, Chiancone E (1994) Identification of the site of ferrocyanide binding involved in the intramolecular electron transfer process to oxidized heme in Scapharca dimeric hemoglobin. *Archives of Biochemistry and Biophysics*, *311*:103–106.

63. Kuss-Petermann M, Wenger OS (2016) Unusual distance dependences of electron transfer rates. *Physical Chemistry Chemical Physics*, *18*: 18657–18664.

64. Gray HB, Winkler JR (2005) Long-range electron transfer. *Proceedings of the National Academy of Sciences*, *102*:3534–3539.

65. Slater JC (1964) Atomic radii in crystals. *The Journal of Chemical Physics*, *41*:3199–3204.

66. Kovina MV, Kochetov GA (1998) Cooperativity and flexibility of active sites in homodimeric transketolase. *FEBS Letters*, *440*:81–84.

67. Kuzmič P (2009) DynaFit—A Software package for enzymology. In *Methods in Enzymology* 467:247-280. Elsevier.

68. Meshalkina LE, Solovjeva ON, Kochetov GA (2011) Interaction of transketolase from human tissues with substrates. *Biochemistry (Moscow)*, *76*:1061–1064.